Coreless Optical Fiber Sensor Based on Surface Plasmon Resonance for Simultaneous Measurement of Magnetic Field and Temperature

Chao Liu, Weiqiang Wang, Jingwei Lv, Famei Wang, Jianxin Wang, Wei Liu, Zao Yi, Miao Liu, Qiang Liu, and Paul K. Chu, *Fellow, IEEE*

***Abstract*—A dual-parameter sensor based on a coreless optical fiber (CF) is designed for the simultaneous detection of magnetic fields (*H*) and temperature (*T*). The side of the CF is polished to form a double D-shape and etched to a certain grove depth on the side surface for gold plating and filling with the magnetic fluid (MF) and polydimethylsiloxane (PDMS). The sensor operates on the principle of surface plasmon resonance (SPR) to achieve magnetic field and temperature sensing. Finite element analysis reveals the modal characteristics of the sensor, showing that the effective magnetic field and temperature detection ranges are 31–200 Oe and 20 °C–80 °C, respectively. The maximum magnetic field sensitivity and temperature sensitivities are 20.207 nm/Oe and −8.423 nm/°C, respectively. Compared to other dual-parameter magnetic field and temperature sensors currently proposed, the magnetic field sensitivity increases by nearly two orders of magnitude, and the temperature sensitivity increases several times. The structure of photonic crystal fiber or antiresonant fiber (ARF) is complex. In contrast, this design offers a simpler structure and fabrication process. The sensor has immense potential in medical diagnosis, environmental detection, and aerospace fields.**

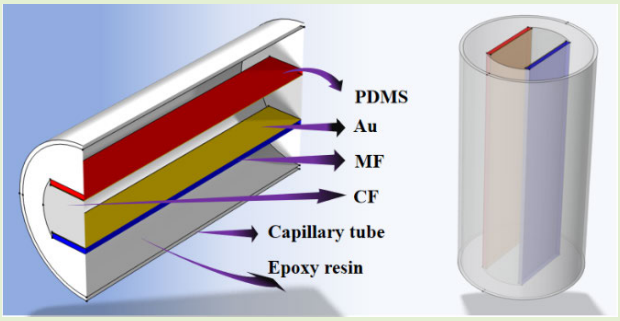

***Index Terms*— Coreless optical fiber (CF), dual-parameter, magnetic field (*H*), simultaneous detection, surface plasmon resonance (SPR), temperature (*T*).**

I. Introduction

TEMPERATURE and magnetic field are key parameters in scientific research and engineering applications, especially navigation, aviation, and climate monitoring [1], [2].

Received 8 March 2025; accepted 31 March 2025. Date of publication 6 May 2025; date of current version 16 June 2025. This work was supported in part by the National Natural Science Foundation of China under Grant 12304480 and Grant 62305223; in part by Heilongjiang Provincial Natural Science Foundation of China under Grant JQ2023F001; in part by the Local Universities Reformation and Development Personnel Training Supporting Project from Central Authorities, Natural Science Foundation of Heilongjiang Province under Grant LH2021F007; in part by China Postdoctoral Science Foundation funded project under Grant 2020M670881; in part by the Natural Science Foundation of Guangdong Province under Grant 2022A1515110971; in part by the Fundamental Project Natural Science Foundation of Heilongjiang Province under Grant LH2022F004; and in part by the City University of Hong Kong Donation under Grant DON-RMG 9229021 and Grant 9220061. The associate editor coordinating the review of this article and approving it for publication was Dr. Anand M. Shrivastav. *(Corresponding author: Chao Liu.)*

Please see the Acknowledgment section of this article for the author affiliations.

Digital Object Identifier 10.1109/JSEN.2025.3562485

Conventional sensors for magnetic field and temperature are based on the resistance change in electrical components such as magneto-transistors, magneto-resistors, and thermistors [3], [4]. Recently, on the heels of the development of optical technology, optical fiber sensors based on surface plasmon resonance (**SPR**) are being used to monitor magnetic field (***H***) and temperature (***T***). SPR occurs when light undergoes total internal reflection on the surface of a metal film, and the evanescent wave that penetrates into the metal film strikes the free electrons inside to form a surface plasmon polariton (**SPP**) wave. Resonance coupling occurs when SPP waves and light waves of a specific wavelength satisfy the phase matching condition. SPR results in the formation of loss peaks in the optical spectrum and their positions are influenced by the refractive index (RI) (***n***) near the metal film [5]. In fact, n of the magnetic fluid (**MF**) or polydimethylsiloxane (**PDMS**) changes with magnetic fields and temperature [6]. Therefore, by embedding sensing materials into the metal-coated optical fiber, it is possible to indirectly detect the magnetic field and temperature by analyzing the changes in the loss peaks.

Hassani and Skorobogatiy [7] have demonstrated the coupling mechanism of SPR-PCF. Compared to electrical sensors, optical fiber sensors have advantages such as high sensitivity, small size, and fast response. Driven by the trend of integration, multiparameter optical fiber sensors are attracting attention. The design of the dual-parameter sensor can be classified into two categories: longitudinal extension that achieves dual-parameter sensing by cascading two single-parameter sensors and lateral extension that realizes dual-parameter sensing functionality by embedding two sensing materials in different areas of the fiber cross section [8].

Xu et al. [9] have proposed an optical fiber sensor for magnetic field and temperature based on the single-mode fiber (SMF)-multimode fiber (MMF)-SMF-hollow core fiber (HCF)-SMF structure. This sensor shows a magnetic field sensitivity of −0.865 dB/mT between 47 and 60 Oe and a temperature sensitivity of 0.519 dB/°C in the range from 27 °C to 43 °C. Fu et al. [10] have designed a cascaded dual-parameter sensor for magnetic field and temperature by wrapping MF and PDMS on the front and back parts of a gold-plated coreless optical fiber (CF). In the range between 0 and 551 Oe, the maximum magnetic field sensitivity is 0.012267 nm/Oe, and in the range between 30 °C and 70 °C, the maximum temperature sensitivity is 1.662.64 nm/°C. Although the cascaded sensor is relatively simple to fabricate, its sensitivity is still low, and the loss is high. Regarding the second type, since it involves embedding sensing materials in different areas of the fiber cross section, most designs are based on PCF by taking advantage of the porosity of PCF to fill the holes with the sensing materials. Zhou et al. [11] have proposed a high-sensitivity PCF-SPR magnetic field and temperature sensor with a gold film inside the air holes in two rows filled with MF and PDMS, showing magnetic field and temperature sensitivities of 0.235 nm/Oe and 2 nm/°C. Owing to the difficult coating process for the optical fiber holes, Liu et al. [12] have designed a gold nanowire-embedded PCF sensor with magnetic field and temperature sensitivities of 0.2384 nm/Oe and 1.1036 nm/°C, respectively. Although the use of gold nanowire reduces the manufacturing difficulty, the magnetic sensitivity is low in addition to a high level of crosstalk. Wang et al. [13] have designed a hexagonal air-hole cladding structure with a gold film inside the PCF holes filled with MF for magnetic field and temperature sensitivities of 0.3125 nm/Oe and 1.993 nm/°C. Besides PCF, antiresonant fibers (ARFs) have been reported. For example, Liu et al. [14] have designed an ARF SPR dual-parameter sensor with magnetic field and temperature sensitivities of 0.3 nm/Oe and 10.8 nm/°C, respectively.

The sensitivity of cascaded dual-parameter sensors is normally low. Since dual-parameter sensors based on PCF and ARF have complex structures, they are difficult to manufacture. Herein, an ultrasensitive bifunctional sensor composed of a CF is designed for the simultaneous detection of magnetic field and temperature. The CF is side-polished into a double D-shape, and grooves with a certain depth are etched into the side-polished surface. The outer surface coated with a gold film is filled with the sensing materials. This approach avoids the difficult coating process and filling inside holes with the sensing medium. The modal characteristics of the sensor are analyzed by COMSOL. The important structural parameters, including the radius of the coreless fiber, the depth of side-polishing, the depth of the groove, and the thickness of the gold film, are optimized. The magnetic field sensitivities of Groove 1 (**Gro 1**) and Groove 2 (**Gro 2**) are 0 and 20.201 nm/Oe, respectively. In the $\boldsymbol{H}$ range from 20 to 200 Oe, the temperature sensitivities are −8.423 and −3.902 nm/°C for Gro 1 and Gro 2, respectively, for $\boldsymbol{T}$ between 20 °C and 80 °C. The cross-sensitivity issue can be resolved by constructing a sensing matrix. Compared to similar sensors recently reported, the magnetic field and temperature sensitivities of our sensor are better by nearly two orders of magnitude and several times, respectively [13], [15], [16]. Furthermore, the sensor is not only structurally simple and easy to manufacture but also has ultrahigh sensitivity, thereby having enormous potential in fields such as medical diagnosis and climate monitoring.

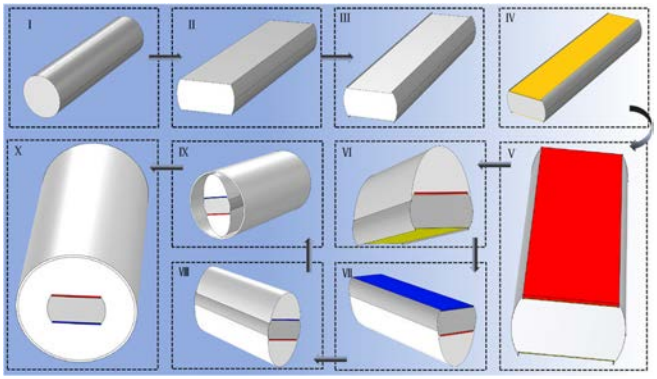

Fig. 1. Manufacturing process of the SPR-COF sensor. (I) CF. (II) Side-throw. (III) Grooving. (IV) Gold-plated film. (V) Fill PDMS. (VI) Cure PDMS. (VII) Fill MF. (VIII) Cure MF. (IX) Sleeve a capillary tube. (X) Fill with epoxy resin.

II. Model and Theory

As shown in Fig. 1(a), the sensor can be manufactured by the following process. A polishing machine is used to side-polish the coreless fiber into a double D-shape, and laser technology is applied to etch grooves with a certain depth on the two side-polished planes. Magnetron sputtering is performed to deposit a gold film on the grooves. After dropping PDMS (with a mixing ratio of 10:1 between PDMS polymer and curing agent) into one of the grooves, use a glass slide or scraper to remove the excess PDMS along the D-plane. Then, use a piece of filter paper to wipe off the excess PDMS along the sidewall of the sensor (alternatively, a glass slide can be placed over the groove, and the PDMS can be drawn into the groove through capillary action. After removing the excess PDMS by rinsing with distilled water, the glass slide can be taken off). A small amount of epoxy resin is then dropped on top for curing as shown in Fig. 1. The same method is used to fill the MF and cure it with epoxy resin, then it is inserted into the capillary tube, and finally, the remaining space inside the capillary tube is filled with epoxy resin [17], [18], [19]. In the cross-sectional structure of the sensor in Fig. 2(a), the radius of the coreless fiber is $\boldsymbol{r}$, the side-polishing depth is $\boldsymbol{h_1}$, and the thickness of PDMS and MF is $\boldsymbol{h_2}$. The thickness of the gold film is $\boldsymbol{h_3}$. The physical

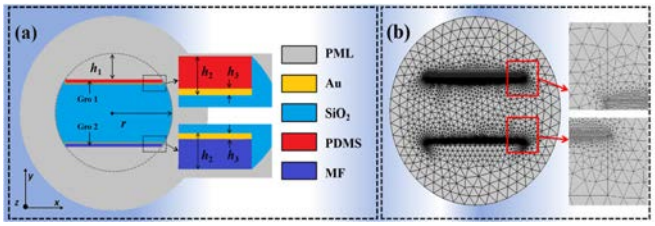

Fig. 2. (a) Cross-sectional structure and (b) grid representation of the SPR-COF sensor.

characteristics of the model are analyzed by the finite element method, and the meshing situation is shown in Fig. 2(b).

The sensor uses gold as the SPR excitation medium. The dielectric constant of gold can be derived from the Drude–Lorentz model [20]

$$\varepsilon_{\mathrm{Au}}(\omega) = \varepsilon_1 + \mathrm{i}\varepsilon_2 = \varepsilon_\infty - \frac{\omega_\mathrm{p}^2}{\boldsymbol{\omega}(\boldsymbol{\omega} + \mathrm{i}\boldsymbol{\omega}_\mathrm{c})} \tag{1}$$

where ε_1 and ε_2 are the real and imaginary parts of the metal dielectric constant, respectively, $\varepsilon_\infty = 9.48$ is the dielectric constant of gold at high frequencies, ω is the angular frequency of the incident light, $\omega_\mathrm{p} = 1.36 \times 1016$ rad/s represents the angular frequency of the plasma, and $\omega_\mathrm{c} = 1.45 \times 1014$ rad/s represents the damping frequency.

The CF is made of SiO_2. Since the sensor is used to detect temperature, it is necessary to consider the effect of temperature on the RI of SiO_2. The Sellmeier equation with temperature is shown in the following [21]:

$$n^2(\lambda, T) = 1.31552 + \mathrm{A}_1 T + \frac{(\mathrm{B}_1 + \mathrm{B}_2 T)\lambda^2}{\lambda^2 - (\mathrm{B}_3 + \mathrm{B}_4 T)} + \frac{(\mathrm{C}_1 + \mathrm{C}_2 T)\lambda^2}{\lambda^2 - 100} \tag{2}$$

where n is the **RI** of SiO_2, $\boldsymbol{\lambda}$ is the wavelength of the incident light, $\boldsymbol{T}$ is the ambient temperature, $\mathrm{A}_1 = 6.90754 \times 10^{-6}$, $\mathrm{B}_1 = 0.788404$, $\mathrm{B}_2 = 2.35835 \times 10^{-5}$, $\mathrm{B}_3 = 0.0110199$, $\mathrm{B}_4 = 0.584758 \times 10^{-6}$, $\mathrm{C}_1 = 0.91316$, and $\mathrm{C}_2 = 0.548368 \times 10^{-6}$.

PDMS, a polymer with strong viscosity, facilitates embedding into the coreless sensor. Compared with ethanol, PDMS has high sensitivity, good mechanical properties, and stability. Its RI is calculated by the following formula [6]:

$$n_{\mathrm{PDMS}} = -4.5 \times 10^{-4} T + 1.4176. \tag{3}$$

MF is a functional material in which changes in temperature and magnetic field cause the movement of magnetic nanoparticles to produce changes in optical properties such as RIs. The RI of MF can be derived from the Langevin model [6]

$$n_{\mathrm{MF}}(n_s - n_0)\left[\coth\left(\alpha\frac{H - H_{c,n}}{T}\right) - \frac{T}{\alpha(H - H_{c,n})}\right] + n_0 \tag{4}$$

where $n_s = 1.4385$ represents the saturated RI of MF, $n_0 = 1.4352$ is the initial RI of MF, $\alpha = 5$ is the fitting coefficient, $H_{c,n} = 30$ Oe represents the magnetic field threshold, and $\boldsymbol{H}$ is the environmental magnetic field.

The SPR phenomenon is dictated by the RI near the excitation medium of gold. When the light within the core and SPP wave satisfy phase matching at a certain wavelength $\boldsymbol{\lambda}$, their effective RIs ($\boldsymbol{n_{\mathrm{eff}}}$) are equal giving rise to resonance. At this point, the light energy in the core can be coupled into the gold film, resulting in a rapid increase in the signal loss transmitted in the fiber. Consequently, a loss peak appears from the loss spectrum, and the loss can be calculated as follows [20]:

$$\alpha_{\mathrm{loss}} = 8.686 \times \frac{2\pi}{\lambda}\mathrm{Im}(\mathrm{n_{eff}}) \times 10^7 \ (\mathrm{dB/cm}) \tag{5}$$

where $\boldsymbol{\lambda}$ is the wavelength of the incident light, and $\mathrm{Im}(\boldsymbol{n_{\mathrm{eff}}})$ is the imaginary part of the effective RI. When SPR occurs, the evanescent wave entering the gold film resonantly couples with the SPP wave. Taking the core mode within the fiber core as an example, the loss spectrum of this core mode reaches an extremum. The wavelength corresponding to this extremum is the resonance wavelength (***RW***). When the temperature or magnetic field of the environment changes, the phase-matching condition also changes, causing a shift in ***RW***. Therefore, the sensitivity of the sensor can be gauged by the change in ***RW***. The RI of the ferrofluid is affected by both the magnetic field and temperature, consequently producing the cross-sensitivity issue. Hence, we need to calculate the temperature sensitivity and magnetic field sensitivity of Gro1 and Gro2 separately [6]

$$S_i(T) = \frac{\Delta\lambda_{\mathrm{peak}i}}{\Delta T}, \quad \text{and} \tag{6}$$

$$\mathrm{S}_i(H) = \frac{\Delta\lambda_{\mathrm{peak}i}}{\Delta H} \tag{7}$$

where $\boldsymbol{S_i(T)}$ and $\boldsymbol{S_i(H)}$ are the temperature sensitivity and magnetic field sensitivity of Gro $\boldsymbol{i}$ ($\boldsymbol{i} = 1, 2$), respectively, $\Delta\boldsymbol{\lambda_{peaki}}$ ($\boldsymbol{i} = 1, 2, 3$) is the wavelength shift corresponding to the peak point $\boldsymbol{i}$ in the loss spectrum, $\Delta\boldsymbol{T}$ is the change in temperature, and $\Delta\boldsymbol{H}$ is the change in the magnetic field. The cross-sensitivity issues can be resolved using a sensitivity matrix [22]

$$\begin{bmatrix}\Delta\lambda_{\mathrm{peak1}} \\ \Delta\lambda_{\mathrm{peak2}}\end{bmatrix} = \begin{bmatrix}S_{\mathrm{Gro1}}(H) & S_{\mathrm{Gro1}(T)} \\ S_{\mathrm{Gro2}}(H) & S_{\mathrm{Gro2}(T)}\end{bmatrix}\begin{bmatrix}\Delta H \\ \Delta T\end{bmatrix} \tag{8}$$

where $\Delta\boldsymbol{\lambda_{peak1}}$ and $\Delta\boldsymbol{\lambda_{peak2}}$ are the shifts of the RW at the extrema of the loss spectrum and $\boldsymbol{S_{Groi}(T)}$ and $\boldsymbol{S_{Groi}(H)}$ ($\boldsymbol{i} = 1, 2$) are the temperature sensitivity and magnetic field sensitivity of Gro 1 and Gro 2, respectively. By inversely solving this relationship, the temperature and magnetic field can be obtained. This process eliminates the cross-sensitivity issue caused by temperature changes

$$\begin{bmatrix}\Delta H \\ \Delta T\end{bmatrix} = \begin{bmatrix}S_{\mathrm{Gro1}}(H) & S_{\mathrm{Gro1}}(T) \\ S_{\mathrm{Gro2}}(H) & S_{\mathrm{Gro2}}(T)\end{bmatrix}^{-1}\begin{bmatrix}\Delta\lambda_{\mathrm{peak1}} \\ \Delta\lambda_{\mathrm{peak2}}\end{bmatrix} \tag{9}$$

where $\boldsymbol{S}$ characterizes the sharpness of loss peaks in the loss spectra and can be calculated as follows:

$$S = \frac{\mathrm{Loss}}{\mathrm{FWHM}} \ (\mathrm{dB}/\mu\mathrm{m}^2)$$

where ***FWHM*** is the full-width at half-maximum of the loss peak [20].

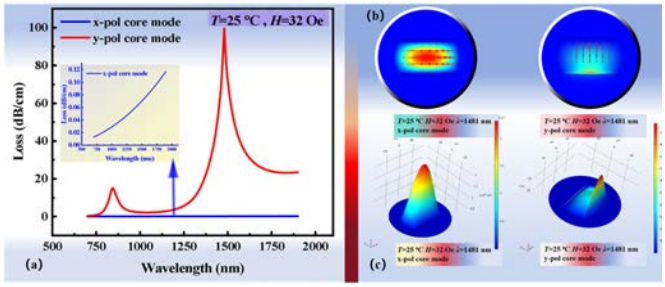

Fig. 3. (a) Loss spectra of the x-pol core mode and y-pol core mode. (b) Electric field distributions of the x-pol core mode and y-pol core mode. (c) 3-D mode field distribution models of x-pol and y-pol.

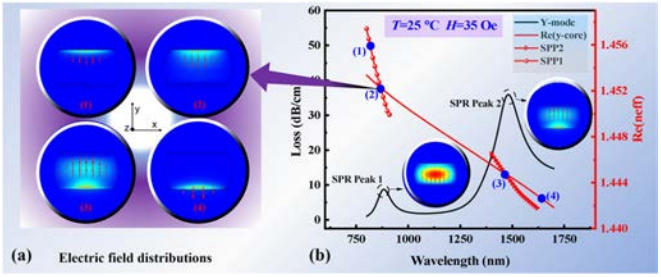

Fig. 4. (a) Electric field distributions of one rank SPP mode and (b) effective RIs of the y-pol core mode and SPP modes and loss spectrum of the SPR-COF sensor.

III. Modal Characteristics

Since the model does not have a rotational symmetry, the x-polarized (**x-pol**) core mode and y-polarized (**y-pol**) core mode have different modal characteristics. As shown in Fig. 3(a), when the temperature is 25 °C and the magnetic field intensity is 32 Oe, the loss spectrum of the y-pol core mode exhibits two distinct loss peaks, while the x-pol core mode does not show any loss peaks and cannot be used for magnetic field and temperature detection. This can be explained by the electric field diagram in Fig. 3(b). From the perspective of the interactions between light and matter, the roles of the electric field and magnetic field in the light wave are not the same. The effect of the magnetic field of the light wave on charged particles in matter is much weaker than that of the electric field of the light wave, so we only analyze the electric fields. The electric field direction of the y-pol core mode is perpendicular to the gold film, thus allowing the energy to couple into the gold film. In comparison, the electric field direction of the x-pol core mode is parallel to the gold film and cannot enter the gold film to interact with the free electrons of the gold film. Fig. 3(c) shows the 3-D electric fields of the x-pol core mode and y-pol core mode, further illustrating the electric field distributions when $\boldsymbol{\lambda} = 1481$ nm. Most of the energy of the y-pol core mode is coupled to the vicinity of the gold film, while the energy of the x-pol core mode is mainly distributed within the core. Therefore, this sensor can be used to detect the magnetic field and temperature by analyzing the y-pol core mode.

Among all the optical wave modes transmitted within the fiber core, the core mode has the shortest cut-off wavelength and the highest corresponding cut-off frequency. When filtering and modulating the optical signal later on, if higher-order modes are analyzed, lower-order modes will definitely exist, which leads to a chaotic optical signal and makes it difficult to find the characteristic values of the optical signal. By setting the cut-off wavelength to the value corresponding to the core mode, only the core mode exists within the sensor, which aids in subsequent signal analysis. In addition, the electric field distribution of the first-order SPP mode is shown in Fig. 4(a), and (1)–(4) are the electric field diagrams of the SPP modes at the four marked points in Fig. 4(b). It can be found that at the wavelengths corresponding to SPR peak 1 and SPR peak 2, the electric field distribution of the SPP mode tends more toward the core, verifying that the SPR phenomenon is excited at this $\boldsymbol{\lambda}$. Moreover, the electric field variation within the fiber cross section is exactly half of a period. This half-period electric field variation image is both simple and can satisfy the requirements for SPR. Therefore, we only analyze the core mode and the first-order SPP mode.

As shown in Fig. 4(b), the effective RI real part [**Re(neff)**] of the y-pol core mode and the Re($\boldsymbol{n_{\text{eff}}}$) of the first-order SPP mode are analyzed as a function of wavelength when $\boldsymbol{H} = 35$ Oe and $\boldsymbol{T} = 25$ °C, along with the loss spectrum of the y-pol core mode. From the figure, it can be seen that there are two loss peaks in the loss spectrum, with an SPR peak 1 at 885 nm and an SPR peak 2 at 1505 nm. The sensor has PDMS filled in Gro 1 and MF filled in Gro 2, making Gro 1 sensitive to temperature and Gro 2 sensitive to the magnetic field. From the inserted electric field diagram in Fig. 4(b), it is observed that there is a significant coupling effect between the y-pol core mode and the gold film, with energy within the core coupling into the gold film. The Re($\boldsymbol{n_{\text{eff}}}$) curves of the SPP mode and the y-pol core mode intersect, and the intersection points are on the same vertical line as the extremum points of the loss peaks, indicating that when the $\boldsymbol{n_{\text{eff}}}$ of the y-pol core mode equals that of the SPP mode, the phase matching condition is satisfied, exciting the SPR phenomenon.

IV. Structural Parameter Optimization

To improve the sensing properties of the sensor, the structural parameters of the model are optimized, namely the CF radius $\boldsymbol{r}$, side etch depth $\boldsymbol{h_1}$, groove depth $\boldsymbol{h_2}$, and gold film thickness $\boldsymbol{h_3}$. The loss spectra are analyzed at a temperature of 25 °C and a magnetic field intensity of 35 Oe. The spacing between the two resonance peaks $\boldsymbol{L_S} = \boldsymbol{RW_{peak2}} - \boldsymbol{RW_{peak1}}$, where $\boldsymbol{RW_{peak2}}$ and $\boldsymbol{RW_{peak1}}$ are the wavelengths corresponding to SPR peak 1 and SPR peak 2, respectively. The total loss of the two resonance peaks $\boldsymbol{b_{TL}} = \boldsymbol{Loss_1} + \boldsymbol{Loss_2}$, where $\boldsymbol{Loss_1}$ and $\boldsymbol{Loss_2}$ are the losses of SPR peak 1 and SPR peak 2, respectively. The total sharpness of the two resonance peaks $\boldsymbol{b_{TS}} = \boldsymbol{S_1} + \boldsymbol{S_2}$, where $\boldsymbol{S_1}$ and $\boldsymbol{S_2}$ are the sharpness values of the two loss peaks, respectively. $\boldsymbol{L_S}$, $\boldsymbol{b_{TL}}$, and $\boldsymbol{b_{TS}}$ are used to evaluate the structural parameters. The greater the distance between the loss peaks, the larger the detection range, the higher the differentiation of the peak signals, the lower the total loss of the two resonance peaks, the higher the efficiency of light transmission, the higher the sharpness of the loss peaks, and the higher the accuracy of discrimination for the SPR peak positions [22].

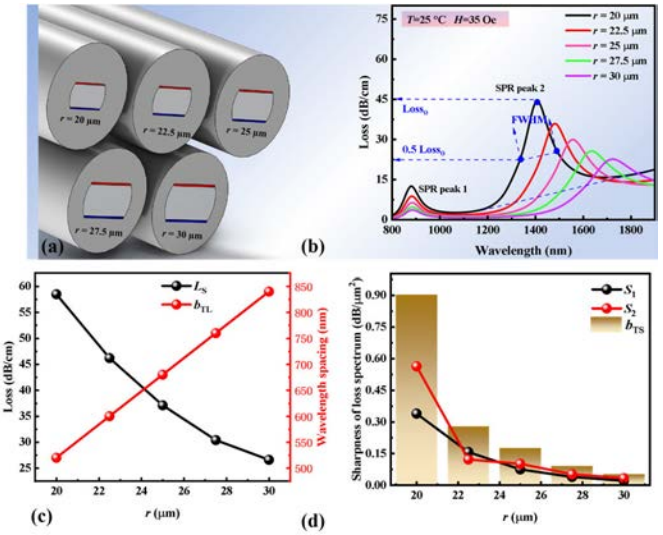

Fig. 5. When $\boldsymbol{r}$ varies between 20 and 30 μm, (a) 3-D model of the sensor, (b) loss spectrum of the sensor, (c) total loss and wavelength spacing of SPR peak 1 and SPR peak 2, and (d) sharpness of the sensor loss peak.

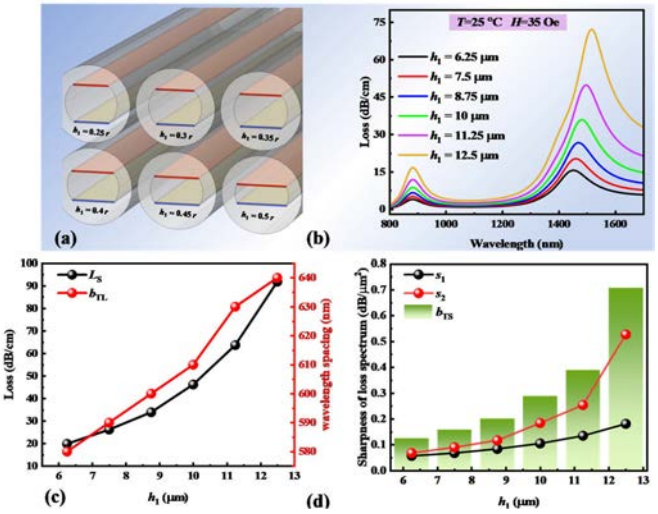

Fig. 6. When $\boldsymbol{h_1}$ varies between 6.25 and 12.5 μm, (a) 3-D model of the sensor, (b) loss spectrum of the sensor, (c) total loss and wavelength spacing of SPR peak 1 and SPR peak 2, and (d) sharpness of the sensor loss peak.

A. CF Radius

The radius of the sensor is optimized. Fig. 5(a) shows the 3-D models of the sensor for different $\boldsymbol{r}$ and other parameters being fixed. The side throw depth $\boldsymbol{h_1}$ is 0.45$\boldsymbol{r}$, the groove depth $\boldsymbol{h_2}$ is 0.065$\boldsymbol{r}$, the gold film thickness $\boldsymbol{h_3}$ is 40 nm, and the $\boldsymbol{r}$ values are 20, 22.5, 25, 27.5, and 30 μm. The loss spectra are shown in Fig. 5(b). For $\boldsymbol{T}$ = 25 °C and $\boldsymbol{H}$ = 35 Oe, as $\boldsymbol{r}$ increases, the loss spectra redshift because the sensor lacks air holes, and the light-guiding area is only SiO_2. When $\boldsymbol{r}$ increases, the change of the RI ($\boldsymbol{n}$) is minimal, mainly due to the increase in the propagation distance of light in the y-direction. As aforementioned, the characteristic of the y-pol core mode is that its electric field changes by half a period ($\boldsymbol{t}$) in the fiber cross section in the y-direction. For $\boldsymbol{v} = c/\boldsymbol{n}$, $\boldsymbol{t} = \boldsymbol{s}/\boldsymbol{v}$, $\boldsymbol{f} = 1/\boldsymbol{t}$, and $\boldsymbol{\lambda} = \boldsymbol{v}/\boldsymbol{f}$ (where c is the speed of light in a vacuum), when $\boldsymbol{r}$ increases, $\boldsymbol{\lambda}$ increases, giving rise to the redshift. The $\boldsymbol{RW}$ of SPR peak 1 becomes smaller, while that of SPR peak 2 changes significantly. This is because $\boldsymbol{n}$ of SiO_2 is about 1.45 RIU, PDMS is about 1.405 RIU, and MF is about 1.435 RIU. The relative $\boldsymbol{n}$ in the central area of the sensor and Gro 1 area is larger, while the relative $\boldsymbol{n}$ in the fiber central axis area and Gro 2 area is smaller. This changes the n distribution since the change of r has a smaller impact on SPR peak 1 and a larger impact on SPR peak 2.

As shown in Fig. 5(c), with increasing $\boldsymbol{r}$, $\boldsymbol{L_S}$ decreases, being 58.3, 46.5, 37.1, 30.4, and 26.6 dB/cm, while $\boldsymbol{b_{TL}}$ increases gradually being 520, 600, 680, 760, and 840 nm. This is because the larger the value of $\boldsymbol{r}$, the higher the value of $\boldsymbol{n_{eff}}$ in the central axis region of the sensor, and light tends to be refracted into the medium with a higher RI. There is less light coupled into the gold film, and the final loss is reduced. As shown in Fig. 5(d), a larger $\boldsymbol{r}$ reduces the total sharpness of the loss peak. After comprehensive consideration, $\boldsymbol{r}$ is chosen to be 25 μm.

B. Depth of Throw

The depth of throw is optimized, and Fig. 6(a) shows the 3-D models of the sensor for different $\boldsymbol{h_1}$, with the other parameters fixed at $\boldsymbol{r}$ = 25 μm, $\boldsymbol{h_2}$ = 0.065$\boldsymbol{r}$, $\boldsymbol{h_3}$ = 40 nm, and $\boldsymbol{h_1}$ values of 6.25, 7.5, 8.75, 10, 11.25, and 12.5 μm. Analyzing the loss spectrum of the sensor, as shown in Fig. 6(b), at $\boldsymbol{T}$ = 25 °C, $\boldsymbol{H}$ = 35 Oe, as the depth of throw $\boldsymbol{h_1}$ increases, the SPR peak 1 does not experience a significant shift, whereas SPR peak 2 undergoes a redshift phenomenon. This occurs because as $\boldsymbol{h_1}$ increases, the proportion of SiO_2 decreases, leading to a reduction in the average RI of the sensor's central area. The frequency f of the y-pol core mode remains constant and since $\boldsymbol{v} = c/\boldsymbol{n}$, $\boldsymbol{\lambda} = \boldsymbol{v}/\boldsymbol{f}$, the wavelength increases. SPR peak 1 does not shift significantly because the large difference in $\boldsymbol{n}$ between PDMS and SiO_2 means that changes in $\boldsymbol{h_1}$ have a minimal effect on the relative RI between Gro 1 and the fiber core, resulting in no significant change in the SPR effect.

As shown in Fig. 6(c), the $\boldsymbol{L_S}$ increases with the increase of $\boldsymbol{h_1}$, being 19.9, 26.2, 33.9, 46.2, 63.7, and 91.8 dB/cm, respectively. The $\boldsymbol{b_{TL}}$ also increases gradually, being 583, 591, 602, 614, 632, and 641 nm, respectively. This is because the larger $\boldsymbol{h_1}$ is, the smaller the distance between the gold film and the central axis of the fiber becomes, which results in a stronger coupling effect between the core mode and the SPP mode, leading to greater loss. As shown in Fig. 6(d), the larger $\boldsymbol{h_1}$ is, the greater the total sharpness of the loss peak becomes, which means higher detection accuracy. After comprehensive consideration, we choose $\boldsymbol{h_1}$ to be 11.25 μm.

C. Depth of Groove

The groove depth is optimized, and Fig. 6(a) shows the 3-D models for $\boldsymbol{h_2}$. The other parameters are fixed except for $\boldsymbol{h_2}$, with $\boldsymbol{r}$ = 25 μm, $\boldsymbol{h_1}$ = 11.25 μm, $\boldsymbol{h_3}$ = 40 nm, and $\boldsymbol{h_2}$ of 1, 1.125, 1.25, 1.375, 1.5, 1.625, and 1.75 μm. The loss spectra are shown in Fig. 7(b). For $\boldsymbol{T}$ = 25 °C, $\boldsymbol{H}$ = 35 Oe, as $\boldsymbol{h_2}$

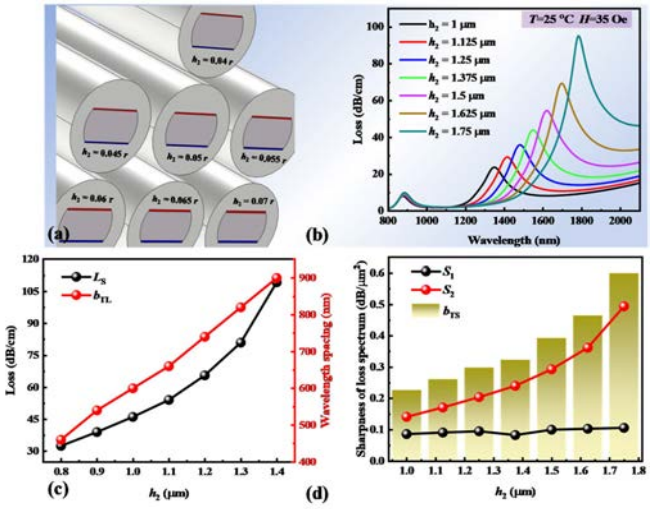

Fig. 7. When h_2 varies between 1 and 1.75 μm, (a) 3-D model of the sensor, (b) loss spectrum of the sensor, (c) total loss and wavelength spacing of SPR peak 1 and SPR peak 2, and (d) sharpness of the sensor loss peak.

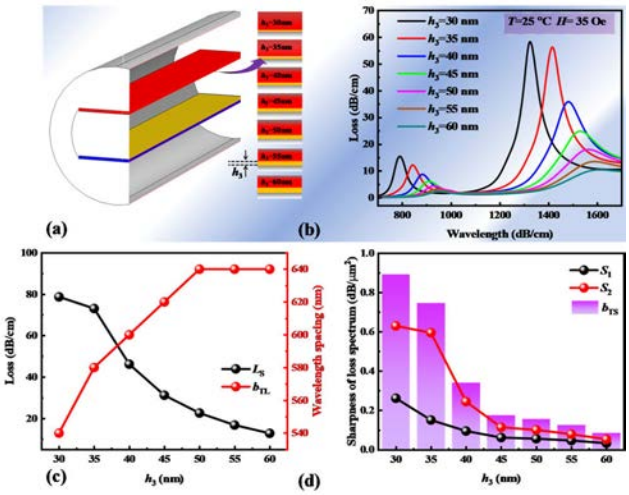

Fig. 8. When h_3 varies between 30 and 60 nm, (a) 3-D model of the sensor, (b) loss spectrum of the sensor, (c) total loss and wavelength spacing of SPR peak 1 and SPR peak 2, and (d) sharpness of the sensor loss peak.

increases, SPR peak 1 does not shift significantly, while SPR peak 2 redshifts, because a larger h_2 leads to more sensing materials being filled, thus lowering the average RI near the gold film. Since $v = c/n$, $\lambda = v/f$, and f remains constant, λ increases, resulting in the redshift. However, the redshift of SPR peak 1 is not significant due to the large difference in RI between PDMS and SiO_2.

As shown in Fig. 7(c), LS increases with increasing h_2, being 32.52, 39.05, 46.18, 54.12, 65.67, 81.03, and 109.35 dB/cm. b_{TL} also increases gradually, being 462, 541, 600, 664, 742, 823, and 902 nm. This is because as h_2 increases, the distance between the gold film and the central axis of the fiber decreases, thus facilitating the coupling between the y-pol core mode and the SPP mode and increasing the loss. As shown in Fig. 7(d), the larger the h_2 value, the greater the total sharpness of the loss peak and the higher the detection accuracy. Considering all the factors, h_2 is chosen to be 1.625 μm.

D. Gold Film Thickness

The thickness of the gold film is optimized. Fig. 8(a) shows the 3-D models for with different h_3 values. The other parameters are fixed: $r = 25$ μm, $h_1 = 11.25$, and $h_2 = 1.625$ μm, while h_3 is varied at 30, 35, 40, 45, 50, 55, and 60 nm. The loss spectra are shown in Fig. 8(b). For $T = 25$ °C and $H = 35$ Oe, h_3 increases, and both resonance peaks redshift because in the wavelength range between 600 and 2000 nm, n of gold is approximately 0.6 RIU. A larger h_3 results in a smaller average RI near the gold film, thus decreasing n_{eff} of the SPP mode. As aforementioned, $v = c/n$ and $\lambda = v/f$, with f remaining constant. It is evident that the resonant λ increases, thus giving rise to the redshift.

As shown in Fig. 8(c), L_S decreases with increasing h_3, being 78.72, 73.15, 46.23, 31.21, 22.66, 16.84, and 12.86 dB/cm. Meanwhile, b_{TL} increases gradually, reaching 540, 580, 600, 620, 640, 642, and 647 nm. This is due to the reduction in n_{eff} of the SPP mode as h_3 increases, thereby resulting in phase matching between the y-pol core mode and the SPP mode. Consequently, n_{eff} of the core mode decreases, and according to the loss (3), the loss decreases. As shown in Fig. 8(d), with increasing h_3, the overall sharpness of the loss peaks and detection accuracy decreases. After considering all the factors, h_3 is chosen to be 35 nm.

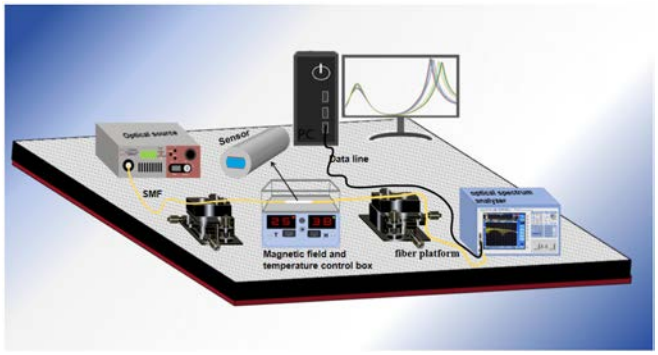

Fig. 9. Schematic of the setup for magnetic field and temperature detection.

V. Magnetic Field and Temperature Sensing

The sensor can achieve simultaneous detection of the magnetic field and temperature using the experimental setup shown in Fig. 9. The SMF is spliced at both ends using a fiber fusion splicer, and the SMF transmits the optical signals. A box with a magnetic field and temperature control is employed to simulate the specific magnetic field and temperature environments. The broadband light source provides the optical signals required for the desired band, and an optical spectrum analyzer (OSA) converts the optical signals into electrical signals and modulates them. The modulated electrical data are analyzed by the PC [23].

Fig. 10 shows the sensing properties of the optimized sensor for magnetic fields. As shown in Fig. 10(a), at $T = 25$ °C,

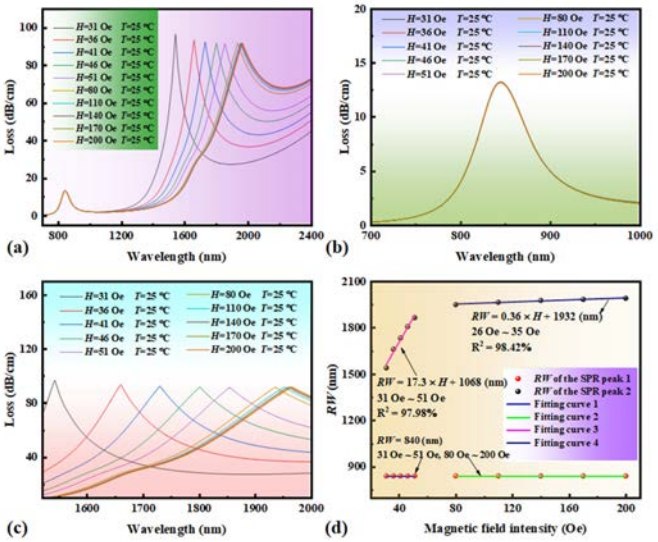

Fig. 10. (a) Loss spectra for different magnetic fields between 31 and 200 Oe. (b) Enlarged loss spectra of SPR peak 1 for different magnetic fields. (c) Enlarged loss spectra of SPR peak 2 for different magnetic fields. (d) Fit results of the ***RW*** shift with magnetic fields.

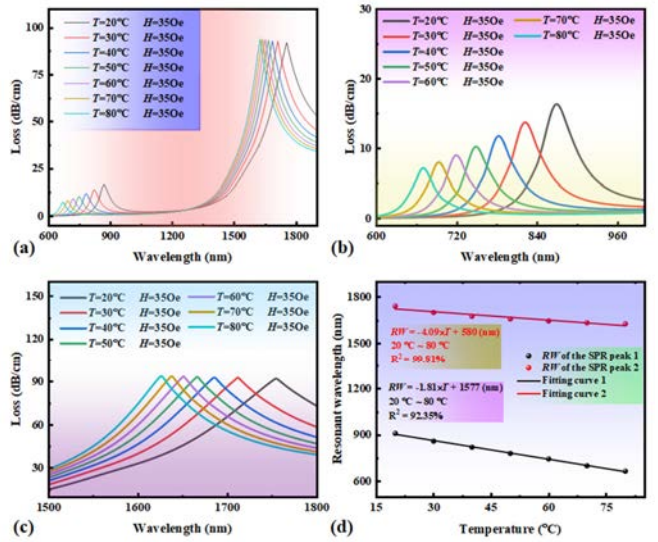

Fig. 11. (a) Loss spectra for temperatures between 20 °C to 80 °C. (b) Enlarged loss spectra of SPR peak 1 for different temperatures. (c) Enlarged loss spectra of SPR peak 2 for different temperatures. (d) Fit results of the ***RW*** shift with temperature.

H varies between 31 and 200 Oe. Fig. 10(b) and (c) is the enlarged loss spectra of the two loss peaks, respectively. When the magnetic field changes, SPR peak 1 does not shift. The RW of the two peaks is linearly fit with ***H***, as shown in Fig. 10(d). The fit curve for SPR peak 1 is a horizontal line, indicating that the magnetic field sensitivity of Gro 1 is 0 nm/Oe. Since the relationship between the interval of RW and ***H*** is nonlinear, the fit curves are plotted for different magnetic field ranges. For SPR peak 2, between 31 and 51 Oe, $\boldsymbol{RW} = 17.3\boldsymbol{H} + 1056$ (nm) with a coefficient of determination (R^2) of 97.98%. Between 80 and 200 Oe, $\boldsymbol{RW} = 0.36\boldsymbol{H} + 1932$ (nm) with $R^2 = 98.42\%$. The magnetic field sensitivity of Gro 2 is higher near $\boldsymbol{H} = 32$ Oe, reaching the maximum of 20.207 nm/Oe.

Fig. 11 shows the temperature-sensing properties of the optimized sensor. Fig. 11(a) shows the results for $\boldsymbol{H} = 35$ Oe and ***T*** between 20 °C and 80 °C. Figs. 10(c) and 11(b) is the enlarged loss spectra of the loss peaks. When the temperature changes, both resonance peaks shift due to the influence of temperature on the magnetic nanoparticles. The ***RW*** of the two peaks is linearly fit with ***T***, as shown in Fig. 11(d). The linearly fit curves of SPR peak 1 are $\boldsymbol{RW} = -4.09\boldsymbol{T} + 580$ (nm) with $R^2 = 99.81\%$, $\boldsymbol{RW} = -1.81\boldsymbol{T} + 1577$ (nm) with $R^2 = 92.35\%$ for 20 °C $\leq \boldsymbol{T} \leq$ 80 °C. The temperature sensitivity is higher near 20 °C, and the highest temperature sensitivity of Gro 1 is calculated to be −8.423 nm/°C. Substituting the average magnetic field sensitivity and average temperature sensitivity of Peak1 and Peak 2 into (9) could obtain the dual-parameter sensing matrix shown as follows. By measuring the wavelength deviation of the Peak 1 and Peak 2, it is possible to demodulate the magnetic field and temperature separately, which addresses the issue of cross-sensitivity caused by temperature variations

$$\begin{cases} \begin{bmatrix} \Delta H \\ \Delta T \end{bmatrix} = \begin{bmatrix} 0 & -4.09 \\ 17.3 & -1.81 \end{bmatrix}^{-1} \begin{bmatrix} \Delta\lambda_{\text{peak1}} \\ \Delta\lambda_{\text{peak2}} \end{bmatrix}, \\ \quad \begin{cases} 31 \text{ Oe} \leq H \leq 51 \text{ Oe} \\ 20 \text{ °C} \leq T \leq 80 \text{ °C} \end{cases} \\ \begin{bmatrix} \Delta H \\ \Delta T \end{bmatrix} = \begin{bmatrix} 0 & -4.13 \\ 0.36 & -1.83 \end{bmatrix}^{-1} \begin{bmatrix} \Delta\lambda_{\text{peak1}} \\ \Delta\lambda_{\text{peak2}} \end{bmatrix} \\ \quad \begin{cases} 80 \text{ Oe} \leq H \leq 200 \text{ Oe} \\ 20 \text{ °C} \leq T \leq 80 \text{ °C}. \end{cases} \end{cases}$$

TABLE I
COMPARISON OF THE PROPERTIES OF DIFFERENT DUAL-PARAMETER SPR OPTICAL FIBER SENSORS FOR MAGNETIC FIELD AND TEMPERATURE SENSING

Refs	Fiber	Detection range	Max magnetic sensitivity	Max temperature sensitivity	Structure
[9]	CF	30 - 70^{0}C 0 - 551 Oe	0.012267 nm/Oe	1.662 nm/^{0}C	
[14]	ARF	20 - 30 ^{0}C 50 -130 Oe	0.3 nm /Oe	10.8 nm/^{0}C	
[23]	MMF	0 -80 ^{0}C 0 -150 Oe	0.217 nm/Oe	-2.26nm/^{0}C	
[12]	PCF	20 - 70^{0}C 30 - 300 Oe	0.2348 nm/Oe	1.1036 nm/°C	
[13]	PCF	/	0.3125 nm/Oe	1.993 nm/°C	
[**This work**]	CF	20 - 80 °C 31 - 200 Oe	20.207 nm/Oe	- 8.423 nm/^{0}C	

To demonstrate the excellent characteristics of the sensor, Table I compares the properties of different magnetic field and temperature sensors. Our sensor shows an improvement in the magnetic field sensitivity by nearly two orders of magnitude and temperature sensitivity by several times.

VI. Conclusion

A dual-parameter sensor based on a CF is designed. In this structure, gold is the excitation source for SPR, and MF and PDMS serve as the sensing materials for the simultaneous detection of magnetic field and temperature. The optimized structural parameters are $\boldsymbol{r} = 25$ μm, $\boldsymbol{h_1} = 11.25$ μm, $\boldsymbol{h_2} = 1.625$ μm, and $\boldsymbol{h_3} = 35$ nm. Numerical analysis reveals that in the magnetic field intensity range between 31 and 200 Oe and temperature range between 20 °C and 32 °C, the sensor exhibits a maximum magnetic field sensitivity of 20.207 nm/Oe and temperature sensitivity of -8.423 nm/°C. Compared to previously reported dual-parameter magnetic field and temperature sensors, the magnetic field sensitivity of our sensor increases by nearly two orders of magnitude, and the temperature sensitivity increases several times.

Acknowledgment

Chao Liu, Weiqiang Wang, Jingwei Lv, Jianxin Wang, Wei Liu, and Qiang Liu are with the School of Physics and Electronic Engineering, Northeast Petroleum University, Daqing 163318, China (e-mail: msm-liu@126.com).

Famei Wang is with Shenzhen Key Laboratory of Ultra-Intense Laser and Advanced Material Technology, Center for Intense Laser Application Technology, and the College of Engineering Physics, Shenzhen Technology University, Shenzhen 518118, China.

Zao Yi is with the Joint Laboratory for Extreme Conditions Matter Properties, Southwest University of Science and Technology, Mianyang 621010, China.

Miao Liu is with the Department of Electronic Information, Northeast Petroleum University, Qinhuangdao 066044, China.

Paul K. Chu is with the Department of Physics, the Department of Materials Science and Engineering, and the Department of Biomedical Engineering, City University of Hong Kong, Hong Kong, China.

References

[1] J. P. Gill and B. K. Taylor, "Navigation by magnetic signatures in a realistic model of Earth's magnetic field," *Bioinspiration Biomimetics*, vol. 19, no. 3, Mar. 2024, Art. no. 036006.

[2] X. Manyosa et al., "MEMS miniaturized low-noise magnetic field sensor for the observation of sub-millihertz magnetic fluctuations in space exploration," *Measurement*, vol. 230, May 2024, Art. no. 114489.

[3] H. Okeil and G. Wachutka, "4H-SiC lateral magnetotransistor with sub-microtesla in-plane magnetic field detectivity," *IEEE Electron Device Lett.*, vol. 45, no. 11, pp. 2173–2176, Nov. 2024.

[4] U. I. Cicek, D. J. Southee, and A. A. Johnson, "The development and characterisation of 3D-printed multi-material thermistor," *Additive Manuf.*, vol. 94, Aug. 2024, Art. no. 104510.

[5] Z. Yin and X. Jing, "Low crosstalk dual-parameter no-core fiber-based SPR sensor with differentiated silver film thickness," *IEEE Sensors J.*, vol. 24, no. 14, pp. 22404–22409, Jul. 2024.

[6] H. Fu et al., "Ultra-high sensitive dual-parameter sensor based on double-hole fiber for simultaneous detection of magnetic field and temperature," *Opt. Exp.*, vol. 32, no. 11, p. 20175, 2024.

[7] A. Hassani and M. Skorobogatiy, "Design criteria for microstructured-optical-fiber-based surface-plasmon-resonance sensors," *J. Opt. Soc. Amer. B, Opt. Phys.*, vol. 24, no. 6, p. 1423, 2007.

[8] M. Hou, Y. Wang, S. Liu, Z. Li, and P. Lu, "Multi-components interferometer based on partially filled dual-core photonic crystal fiber for temperature and strain sensing," *IEEE Sensors J.*, vol. 16, no. 16, pp. 6192–6196, Aug. 2016.

[9] R. Xu et al., "Simultaneous measurement of magnetic field and temperature based on SMF-MMF-SMF-HCF-SMF fiber structure," *IEEE Sensors J.*, vol. 24, no. 4, pp. 4549–4556, Feb. 2024.

[10] J. Fu et al., "Reflective magnetic field and temperature dual-parameter sensor based on no-core fiber probe," *Opt. Laser Technol.*, vol. 174, Jul. 2024, Art. no. 110550.

[11] W. Zhou, X. Qin, M. Lv, L. Qiu, Z. Chen, and F. Zhang, "Design of plasmonic photonic crystal fiber for highly sensitive magnetic field and temperature simultaneous measurement," *Micromachines*, vol. 14, no. 9, p. 1684, Aug. 2023.

[12] J. Liu et al., "Design of a gold-nanowires embedded PCF for magnetic field and temperature sensing," *Plasmonics*, vol. 2024, pp. 1–10, Aug. 2024.

[13] G. Wang et al., "Temperature and magnetic field fiber sensor with high sensitivity and linearity based on surface plasmon resonance," *Opt. Commun.*, vol. 574, Jan. 2025, Art. no. 131140.

[14] M. Liu, X. Leng, W. Ni, and P. P. Shum, "Simultaneous and ultra-sensitive measurement of refractive index and temperature based on SPR of hollow-core anti-resonant fibers," *Plasmonics*, vol. 19, no. 6, pp. 3091–3100, Feb. 2024.

[15] R. Pan et al., "A deep-learning-assisted fiber-optic sensor capable of simultaneously measuring temperature and vector magnetic field," *IEEE Sensors J.*, vol. 24, no. 19, pp. 30128–30135, Oct. 2024.

[16] C. Zhang et al., "Simultaneous measurement of bidirectional magnetic field and temperature with a dual-channel sensor based on the whispering gallery mode," *Opt. Exp.*, vol. 32, no. 11, p. 19541, 2024.

[17] V. Genovés, L. Maini, C. Roman, C. Hierold, and N. Cesarovic, "Variation in the viscoelastic properties of polydimethylsiloxane (PDMS) with the temperature at ultrasonic frequencies," *Polym. Test.*, vol. 124, Jul. 2023, Art. no. 108067.

[18] Z. Cai, H. Song, Z. Zhang, and X. Yao, "Cryogenic temperature characteristics of thermosetting epoxy resins coated FBG sensors," in *Proc. IEEE Sensors Appl. Symp. (SAS)*, Aug. 2021, pp. 1–5.

[19] B. Sanipatin, L. A. Sánchez, L. Arques, and S. Sales, "Microsphere-augmented PDMS integration in tapered FBG small-scale sensors for enhanced temperature sensitivity," *Sci. Rep.*, vol. 14, no. 1, p. 29376, Nov. 2024.

[20] J. Wang et al., "Ultra-high sensitivity photonic crystal fiber sensor based on dispersion turning point sensitization of surface plasmonic polariton modes for low RI liquid detection," *Opt. Exp.*, vol. 32, no. 19, p. 32895, Sep. 2024.

[21] R. Xu et al., "Symmetrical dual-D and dual-core single-mode fiber surface plasmon resonance liquid sensor," *J. Opt. Soc. Amer. A, Opt. Image Sci.*, vol. 41, no. 8, p. 1469, Aug. 2024.

[22] D. Wang et al., "Two-channel photonic crystal fiber based on surface plasmon resonance for magnetic field and temperature dual-parameter sensing," *Phys. Chem. Chem. Phys.*, vol. 24, no. 35, pp. 21233–21241, 2022.

[23] H. Li, R. Fu, X. Yan, T. Hu, H. Tang, and T. Cheng, "Dual-channel high-sensitivity temperature and magnetic field sensor based on Mach–Zehnder interference and surface plasmon resonance," *IEEE Sensors J.*, vol. 24, no. 22, pp. 36768–36775, Nov. 2024.